Solution Structure and Backbone Dynamics of the Defunct Domain of Calcium Vector Protein†

Isabelle Théret,‡ Sibyl Baladi,§ Jos A. Cox,§ Jacques Gallay,|| Hiroshi Sakamoto,⊥ and Constantin T. Craescu*,‡

INSERM U350 and Institut Curie-Recherche, Centre Universitaire, Bâtiments 110-112, 91405 Orsay Cedex, France, Département de Biochimie, Université de Genève, Genève, Switzerland, LURE, Orsay, France, and Institut Pasteur, Paris, France

Received July 11, 2001; Revised Manuscript Received August 29, 2001

ABSTRACT: CaVP (calcium vector protein) is a Ca^{2+} sensor of the EF-hand protein family which is highly abundant in the muscle of *Amphioxus*. Its three-dimensional structure is not known, but according to the sequence analysis, the protein is composed of two domains, each containing a pair of EF-hand motifs. We determined recently the solution structure of the C-terminal domain (Trp81−Ser161) and characterized the large conformational and dynamic changes induced by Ca^{2+} binding. In contrast, the N-terminal domain (Ala1−Asp86) has lost the capacity to bind the metal ion due to critical mutations and insertions in the two calcium loops. In this paper, we report the solution structure of the N-terminal domain and its backbone dynamics based on NMR spectroscopy, nuclear relaxation, and molecular modeling. The well-resolved three-dimensional structure is typical of a pair of EF-hand motifs, joined together by a short antiparallel β-sheet. The tertiary arrangement of the two EF-hands results in a closed-type conformation, with near-antiparallel α-helices, similar to other EF-hand pairs in the absence of calcium ions. To characterize the internal dynamics of the protein, we measured the ^{15}N nuclear relaxation rates and the heteronuclear NOE effect in ^{15}N-labeled N-CaVP at a magnetic field of 11.74 T and 298 K. The domain is mainly monomeric in solution and undergoes an isotropic Brownian rotational diffusion with a correlation time of 7.1 ns, in good agreement with the fluorescence anisotropy decay measurements. Data analysis using a model-free procedure showed that the amide backbone groups in the α-helices and β-strands undergo highly restricted movements on a picosecond to nanosecond time scale. The amide groups in Ca^{2+} binding loops and in the linker fragment also display rapid fluctuations with slightly increased amplitudes.

Calcium vector protein (CaVP)[1] is a Ca^{2+} binding protein isolated (*1*) from the muscle of a protochordate, *Amphioxus* (commonly called lancelet fish), but it is also expressed in the spinal chord and the gonads. Due to several vertebrate traits, this marine animal is believed to constitute the evolutionary link between invertebrates and vertebrates (*2*). In situ, CaVP forms a tight complex with its natural target, a protein of 26.6 kDa named the calcium vector protein target (CaVPT) (*3*). Only two of the four EF-hand motifs are active, with very different intrinsic binding constants ($K'_{Ca1} = 4.9 \times 10^6$ M^{-1} and $K'_{Ca2} = 7.3 \times 10^3$ M^{-1}) which depend strongly on the interaction with the target (*4*). Despite the large body of biochemical information about the isolated proteins, the physiological role of the unique CaVP−CaVPT complex is still incompletely clarified.

With its four EF-hand motifs, CaVP belongs to an ensemble of congruent EF-hand proteins from the TnC superfamily, including calmodulin, troponin C, and essential and regulatory light chains, with a similar genetic evolution pattern (*5*, *6*). Comparative sequence analysis and molecular modeling (*7*) suggested that CaVP is composed of two independent folding modules linked by a central α-helix. This hypothesis is supported by recent experimental studies, conducted in our laboratory, which demonstrated the structural autonomy of the two half-domains (*8*, *9*). We also showed that the two active binding sites are situated in the C-terminal domain (*9*), and that sequential metal ion binding is accompanied by large structural and dynamic changes (*8*).

Sequence comparison of the N-terminal domain of CaVP (N-CaVP) with the corresponding domain of CaM or TnC (Figure 1) points to several critical sequence alterations within the calcium binding loops which should be responsible for the lack of ion binding (*10*). In the first Ca^{2+} binding loop, substitution of a Pro at position $-X$ for an oxygen-bearing side chain and the Asp for Glu substitution at position $-Z$ decrease the number of potential ion ligands and the optimal binding geometry, respectively. In the second loop, insertion of two residues and nonconservative substitutions of four side chains among the ion ligands (boxed in Figure 1) may completely abolish Ca^{2+} binding. Recent studies showed that presence of residues with small side chains in

† This work was supported by the Centre National de la Recherche Scientifique, the Institut Curie, and the Swiss National Science Foundation.

* To whom correspondence should be addressed. Phone: 33 1 69 86 31 63. Fax: 33 1 69 07 53 27. E-mail: gil.craescu@curie.u-psud.fr.

‡ Centre Universitaire.

§ Université de Genève.

|| LURE.

⊥ Institut Pasteur.

[1] Abbreviations: CaM, calmodulin; CaVP, calcium vector protein; N-CaVP, N-terminal domain of CaVP (residues 1−86); C-CaVP, C-terminal domain of CaVP (residues 81−161); CaVPT, calcium vector protein target; TnC, troponin C; DTT, dithiothreitol

10.1021/bi011444q CCC: $20.00
Published on Web 10/26/2001

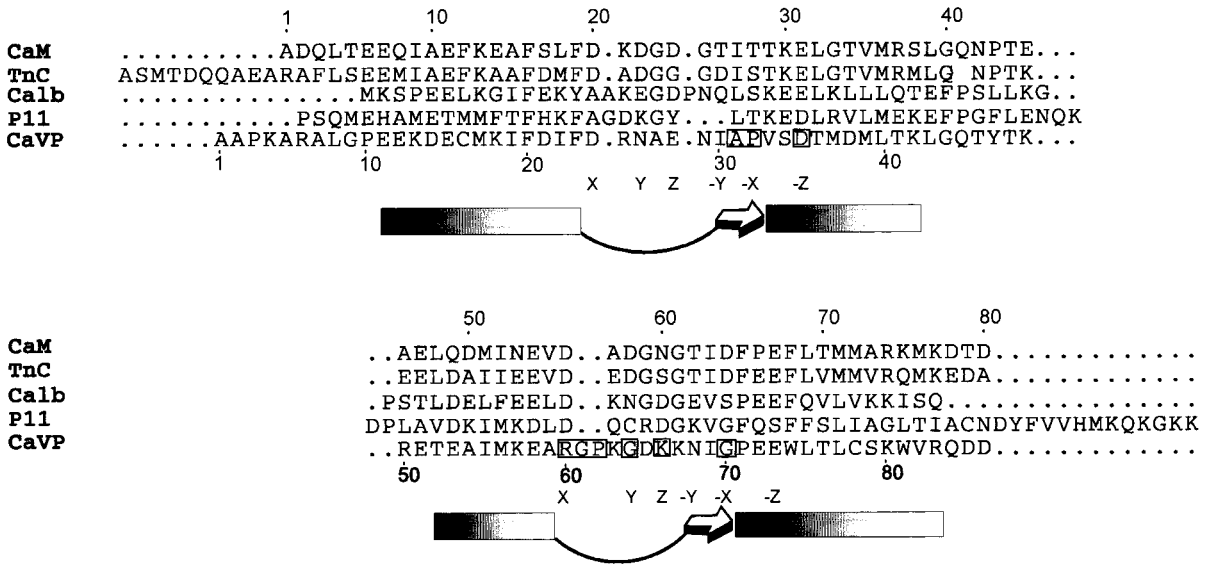

FIGURE 1: Sequence comparison of the N-terminal domains of CaM, TnC, bovine calbindin D_{9k}, p11 (S100A10), and CaVP. Residues directly involved in Ca^{2+} binding in the consensus sequence are labeled with *X*, *Y*, *Z*, $-Y$, $-X$, and $-Z$, according to their positions in a pentagonal bipyramid. The secondary structure elements determined in this work for N-CaVP are shown under the sequences. Insertions and unfavorable substitutions in the binding loops of N-CaVP are shown in boxes.

the middle of β-strands leads to a substantial reduction of the Ca^{2+} affinity (*11*, *12*) by decreasing the stability of the hydrophobic core in both the apo and holo forms. Therefore, the presence of Ala31 in loop I constitutes an additional unfavorable factor for Ca^{2+} binding.

Overexpression in large quantities of N-CaVP permitted us to demonstrate that, despite a stable structural organization, the domain has indeed lost its ion binding capacity. In addition, N-CaVP alone is not able to recognize the CaVPT but seems to modulate and increase the affinity of the whole protein for its target (*9*). Understanding of the role played by the amino-terminal lobe of CaVP in recognition and binding of the target protein requires determination of its three-dimensional structure, in the isolated form or in the intact protein. We report here the solution structure of the isolated N-CaVP domain, determined by NMR spectroscopy and molecular modeling. Our results showed that, independent of the presence of Ca^{2+} ions, the domain has a regular fold, similar to those of other stable apo domains, with the four α-helices forming a near-antiparallel helix bundle. ^{15}N spin relaxation studies at 298 K of N-CaVP allowed us to characterize the internal backbone dynamics on the picosecond to nanosecond time scale, using a model-free procedure. Contrary to the Ca^{2+}-loaded C-terminal domain (C-CaVP) (*13*), we found no evidence for localized slow conformational exchange. Comparison with the previous results on holo C-CaVP permits us to delineate the structural and dynamic differences between the two domains and to discuss the possible functional role of the nonbinding N-terminal domain.

MATERIALS AND METHODS

Sample Preparation. N-CaVP (Ala1−Asp86) was overexpressed in *Escherichia coli* and purified as described previously (*9*). ^{15}N labeling was performed in an M63 medium containing appropriate antibiotics and $(^{15}NH_4)_2SO_4$ (2 g/L) as the sole source of nitrogen. The NMR samples, in the concentration range of 0.8−1.7 mM, were dissolved in deuterated Tris buffer (20 mM, pH 6.5) containing 100 mM KCl, 0.5 mM DTT, and 5 mM $CaCl_2$.

Experimental Procedures. All NMR spectra were acquired on a Varian Unity500 NMR spectrometer equipped with a triple probe and a *Z*-field gradient. Assignment of ^1H and ^{15}N resonances was achieved by analyzing the following set of two- and three-dimensional NMR spectra: NOESY (150 ms mixing time), TOCSY (60 and 110 ms mixing times), COSY-DQF, $\{^1H-^{15}N\}$ HSQC, NOESY-HSQC (100 ms mixing time), and TOCSY-HSQC (*14*). The three-dimensional spectra were recorded with a spectral width of 7000 Hz in the proton dimensions and 1500 Hz in the ^{15}N dimension. The acquisition was achieved with 2048 complex points in t_3, and with 128 and 32 increments in t_1 and t_2, respectively. Spectra analysis and restraint collection were carried out using FELIX 3.0 (MSI, San Diego, CA). The baseline correction was carried out on the two- and three-dimensional spectra using the FACELIFT program (*15*).

Structure Calculations. Interproton distance restraints were obtained from the NOESY-HSQC spectrum for the amide protons and from the NOESY (in ^2H_2O) for the side chain−side chain interactions. The peak intensities were calibrated relative to NOEs corresponding to known interproton distances such as the H^N-H^N (2.8 Å in an α-helix) and $H^{\beta1}-H^{\beta2}$ (1.8 Å in methylene groups) distances. The NOE restraints were classified into three categories: strong, medium, and weak, corresponding to interproton distance ranges of 1.8−2.9, 2.9−3.7, and 3.7−5.0 Å, respectively, with the exception of $d_{\alpha N}(i, i+1)$, $d_{NN}(i, i+1)$, $d_{\alpha N}(i, i+2)$, and $d_{NN}(i, i+2)$ in helical secondary structures which fall into ranges of 3.3−3.7, 2.6−3.0, 4.2−4.6, and 4.0−4.4 Å, respectively.

A total of 844 distance constraints, including 194 intraresidue, 245 sequential, 190 medium-range ($2 < |i-j| < 5$), and 215 long-range ($|i-j| \geq 5$), were finally used for the structure calculation (Table 1). An additional 104 dihedral restraints and 62 hydrogen bonds, derived from vicinal coupling constants and secondary structure considerations,

Table 1: Restraint and Structural Statistics for the 31 Simulated Annealing Structures of N-CaVP (Ala1−Asp86)

restraint statistics		
no. of NOE restraints	844	
intraresidue	194	23%
sequential	245	29%
medium-range ($2 \leq \|i-j\| < 5$)	190	23%
long-range ($\|i-j\| \geq 5$)	215	25%
no. of hydrogen bond restraints	62	
no. of dihedral angle restraints (Φ and Ψ)	104	
average no. of NOE restraint violations		
>0.6 Å	none	
>0.4 Å	1.7/structure	
rmsd from experimental distance restraints (Å)	0.061 (0.005)	
rmsd from experimental dihedral restraints (deg)	3.08 (0.83)	
rmsd from idealized geometry		
bonds (Å)	0.010 (0.008)	
angles (deg)	2.14 (0.05)	

	av rmsd (Å) from the av structure	av pairwise rmsd (Å)
residues 11−23, 30−42, 52−59, and 68−83[a]	0.53 (0.07)	0.75 (0.05)
residues 11−23, 30−42, 52−59, and 68−83[b]	1.47 (0.10)	2.11 (0.24)
helices 1 and 2, β-strand[a]	0.47 (0.08)	0.67 (0.14)
helices 3 and 4, β-strand[a]	0.47 (0.09)	0.66 (0.17)
helix 1[a]	0.37 (0.11)	
helix 2[a]	0.19 (0.03)	
helix 3[a]	0.15 (0.05)	
helix 4[a]	0.40 (0.13)	

[a] Backbone atoms (N, C′, and Cα). [b] All atoms. Φ and Ψ in the most favored region (75.7%).

were included. No explicit restraint were employed for the eventual disulfide bridge.

Starting from an extended structure and after several iterations under NMR restraints of the distance geometry program (DGII), aimed to improve the quality of the experimental information, we generated 100 structures, 65 of which converged properly and exhibited a low final error function. Refinement of these last structures (under the same restraint file minus the hydrogen bonds) was carried out with the simulated annealing protocol and the cvff force field of Discover (maximal temperature of 1200 K and a final temperature of 300 K). A final set of 31 structures, selected on the basis of the lowest-energy and the minimal restraint violations, were retained. The AQUA and PROCHECK-NMR programs (*16*) were used to analyze the restraint violations and to estimate the precision and quality of the obtained structures.

The atomic coordinates of the 31 best structures and of the energy-minimized average structure were deposited in the Protein Data Bank as entries 1J7Q and 1J7R, respectively.

^{15}N Relaxation Measurements. Experiments were carried out at 298 K at 11.74 T. The R_1 (^{15}N spin−lattice) and R_2 (spin−spin) relaxation rates and the NOE (steady-state $\{^1H\}-^{15}N$ nuclear Overhauser effect) were measured with the pulse sequences provided by L. E. Kay (*17*). Relaxation delays for the R_1 spectra were fixed to 11.044 (twice), 55.22, 165.66, 220.88 (twice), 386.88, 552.2, 662.64, 828.3, and 1104.4 ms. The spectra for R_2 measurements were acquired using 15.7, 31.4, 47.1, 62.8 (twice), 78.5, 94.2, 125.6, 157, 188.4, and 219.8 ms delays. The steady-state $\{^1H\}-^{15}N$ nuclear Overhauser effect (NOE) was determined from spectra pairs recorded with and without proton saturation. NMR experiments were recorded with 2048 complex points and a spectral width of 7000 Hz in t_2 and with 96 complex points and a spectral width of 1500 Hz in t_1. The relaxation data were processed using a specialized routine of FELIX 3.0 software. A squared sine-bell window function shifted by 90° was applied in t_2 and a sine-bell window function shifted by 90° in t_1. The final matrix size was 1024 × 512 real points after Fourier transformation.

Relaxation rates R_1 and R_2 and their uncertainties were determined by least-squares fitting of the measured peak heights to a two-parameter exponential decay via an in-house computer program. The heteronuclear steady-state NOE values were determined from the ratio of the peak intensities obtained with and without ^1H saturation. The NOE effect is given by the equation $\eta = \mathrm{NOE} - 1$. Estimation of NOE uncertainties was based on uncertainties of the peak heights and the law of uncertainties propagation.

The Lipari−Szabo approach for the relaxation data analysis assumes that the overall rotation of the molecule and the internal motions of the bonds vectors, which both contribute to the spin relaxation, are independent and their contributions to the total spectral density function at any frequency are additive (*18*):

$$J(\omega) = \frac{2}{5}\left[\frac{S^2\tau_c}{1+(\omega\tau_c)^2} + \frac{(1-S^2)\tau_i}{1+(\omega\tau_i)^2}\right] \quad (1)$$

where τ_c is the global correlation time, τ_i is given by the relation $1/\tau_i = 1/\tau_e + 1/\tau_c$ (where τ_e is the local effective correlation time describing the fast motion), S^2 is the generalized order parameter, which depends on the amplitude of the local H^N-N bond motion on the picosecond to nanosecond time scale. In a more complex formalism (*19*), the spectral density function for an isotropic motion can be described as a sum of three contributions:

$$J(\omega) = \frac{2}{5}\left[\frac{S^2\tau_c}{1+(\omega\tau_c)^2} + \frac{(1-S_f^{\,2})\tau_f'}{1+(\omega\tau_f')^2} + \frac{(S_f^{\,2}-S^2)\tau_s'}{1+(\omega\tau_s')^2}\right]$$

where S^2 ($=S_f^2S_s^2$) is the square of the generalized order parameter and S_f^2 and S_s^2 are the order parameters corresponding to the fast and slow internal motions, respectively, with the effective characteristic time constants τ_f and τ_s ($1/\tau_x' = 1/\tau_x + 1/\tau_c$).

The first step in the dynamics analysis was the estimation of the global rotational correlation time τ_c, using a procedure specifically designed to minimize the unsuitable effects of the slow motions (*20*). Fitting the R_{1exp} and NOE_{exp} values for amides groups in well-structured regions, at a given τ_c, one can reconstruct the R_{2cal} values and compare them with the corresponding experimental values. The optimum correlation time corresponds to the R_{2cal} obtained by minimizing the χ^2 function:

$$\chi^2 = \sum_{\text{residues}} \frac{(R_{2exp} - R_{2cal})^2}{\sigma^2(R_2)}$$

Time-Resolved Fluorescence Measurements. Fluorescence intensity and anisotropy decays were obtained with a time-correlated single-photon counting technique from the $I_{vv}(t)$ and $I_{vh}(t)$ components recorded on the experimental setup installed on the SB1 window of the synchroton radiation

machine Super-ACO (Anneau de Collision d'Orsay, Orsay, France), which was described previously (*21*). The excitation wavelength was selected by a double monochromator (Jobin Yvon UV-DH10, bandwidth of 4 nm). An MCP-PMT Hamamatsu (model R3809U-52) detector was used. The time resolution was ~11 ps, and the data were stored in 2048 channels. Automatic sampling cycles, including a 30 s accumulation time for the instrument response function and a 90 s acquisition time for each polarized component, were carried out until a total number of $2-4 \times 10^6$ counts were reached in the fluorescence intensity decay. Analyses of the fluorescence intensity and anisotropy decays as sums of exponentials were performed according to the maximum entropy method, as described previously (*22*). Samples were 10 μM in Tris buffer (20 mM, pH 6.5) containing 0.5 mM DTT and 100 mM KCl.

RESULTS AND DISCUSSION

Experimental Conditions and Spectral Assignment. The length of the overexpressed N-terminal domain was chosen so as to cover the first two EF-hand motifs, as suggested by sequence comparison with other proteins from the TnC subfamily (Figure 1). Preliminary NMR studies showed that at higher (nondenaturing) temperatures the line width of the proton resonances becomes larger and the quality of the two-dimensional spectra is significantly decreased. One possible explanation is that N-CaVP has a propensity to form dimers via hydrophobic interactions, which is usually enhanced by the temperature. This hypothesis is not supported by ultracentrifugation experiments which showed that at concentrations of 100 μM the protein is essentially in a monomeric form. Therefore, the existence of slightly different conformations fluctuating at intermediate rates on the NMR time scale may explain the spectral features described above. Low temperatures may stabilize more compact and less fluctuating conformations as was equally observed for the apo regulatory domain of skeletal muscle TnC (*23*). Consequently, the NMR spectra were recorded at 25 °C, a compromise solution between the temperature-dependent effects on rotational diffusion and molecular flexibility. The spectral properties were not sensitive to Ca^{2+} (up to 10 mM), but 100 mM KCl significantly improved the line width.

The assignment of proton and nitrogen resonances was obtained using homonuclear two-dimensional and heteronuclear three-dimensional NMR experiments for spin system identification and sequential assignment. The two-dimensional DQ spectrum (*24*) was useful for a straightforward identification of the five glycine spin systems. Resonances corresponding to the N-terminal end (Ala1−Pro3) give poor NOE connectivities, probably due to an increased flexibility, and remain unassigned. In the remaining sequence (Lys4−Asp86), we were not able to identify unambiguously three amino acids (Lys49, Arg50, and Lys67) probably due to unusual line broadening. Lys49 and Arg50 are situated in the hinge region between the linker and the third α-helix. Similarly, Lys67 is located in the second calcium binding loop, which may be a flexile segment in the absence of the metal ions. The four assigned Pro residues were shown to form trans peptide bonds with the previous residues.

The well-dispersed HSQC spectrum (Figure 2) indicates that even in absence of bound Ca^{2+} ions, N-CaVP assumes

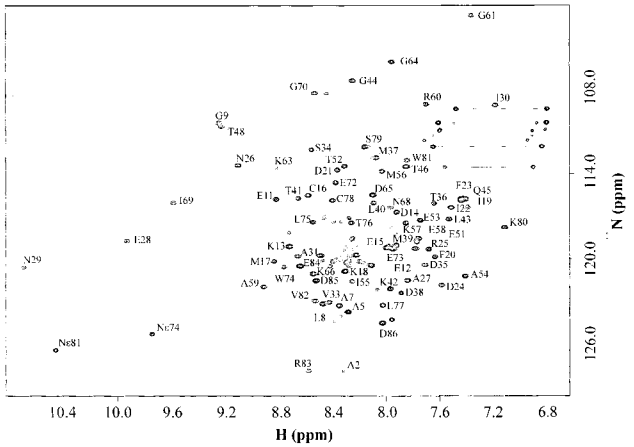

FIGURE 2: Two-dimensional {$^{15}N-^{1}H$} HSQC spectrum of N-CaVP recorded at 500 MHz and 25 °C. Assignment of the amide groups is indicated by the amino acid type and number.

a unique and persistent three-dimensional fold. The amide proton of Asn29, in the sixth position of loop I, is significantly low-field shifted (10.7 ppm) relative to the other amide proton resonances. The glycine residue, usually encountered in this position of EF-hand proteins (*10*), exhibits large chemical shifts, which were rationalized by the existence of a hydrogen bond between the Gly amide proton and one of the carboxyl oxygens of the Asp in position 1 of the loop (*25*). Such an intraloop bond is usually considered a characteristic of a structured Ca^{2+}-bound helix−loop−helix motif, but it was also observed in the absence of any bound ion [sites I and II in sTnC (*26*), site II in cTnC (*27*), sites I−III of CaM (*28*), and the C-terminal EF-hand of calbindin D_{9k} (*29*)]. This feature, revealed by the chemical shift analysis, was confirmed by a recent comparison of the internal dynamics profiles in various binding loops (*30*).

In contrast with the first motif, the sequence of the second calcium loop is more distant from the consensus sequence. Thus, positions 1 and 6 in the loop are occupied by Arg60 and Lys67, respectively. An Arg residue is highly unusual in position 1 (*10*), and contrary to the aspartate residue found in this position in a large majority (99%) of cases, its side chain cannot provide carboxyl oxygens, necessary for the hydrogen bonds and metal chelation. Lys67 remained unassigned, but it is unlikely that its H^N resonates in the low-field spectral region, in the vicinity of the H^N-N peak of Asn29.

Another spectroscopic sensitive probe for Ca^{2+} binding to a loop (*31*) refers to the amide ^{15}N chemical shift of the residue in position 8. Generally, the metal binding induces a considerable deshielding of the corresponding nitrogen nucleus by 4−8 ppm relative to the apo form. This rule is also satisfied here, in the case of a defunct EF-hand domain; the corresponding values in the metal-free N-CaVP for Ala31 and Ile69 are 119.8 and 116 ppm, respectively, which are 4−8 ppm lower in field compared to the corresponding residues (Ile105 and Ile142) in the bound C-CaVP domain.

Secondary Structure and Experimental Restraints. The secondary structure elements were first delineated by a combined analysis of short- and medium-range NOE connectivities between backbone protons, and of the chemical shift index of H^α protons (*32*). Four α-helices were defined with the following limits: Glu11−Phe23 (A), Val33−Lys42

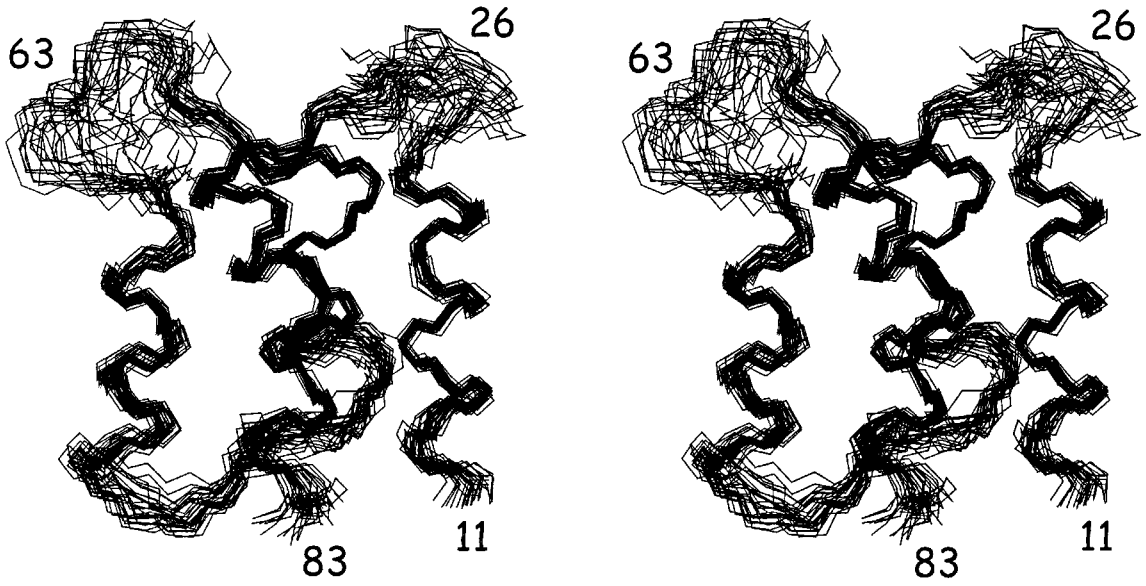

FIGURE 3: Stereoview of the best superimposition of the 31 final structures of N-CaVP at 25 °C. The backbone atoms (N, C′, and Cα) in secondary structure elements were used for the optimization of the superposition.

(B), Glu52−Ala59 (C), and Pro71−Arg83 (D). The α-helical content (51%) is in good agreement with that predicted from the circular dichroism experiments (48%) (*9*). Within each calcium binding loop (Asp24−Asp35 and Pro62−Glu73), two short *β*-strands were clearly identified from the downshift of H^{α} resonances and the strong sequential $d_{\alpha N}(i, i + 1)$ connectivities. They form an antiparallel *β*-sheet, as indicated by the strong dipolar interactions between opposite H^{α} protons: H^{α}(Ile30)−H^{α}(Gly70) and H^{α}(Pro32)−H^{α}(Asn68). The first seven residues and the last two residues in the sequence show no NOE connectivity and appear to explore a large conformational space.

Tertiary Structure. The quality and precision of the 31 best structures, which were finally retained, were assessed by the analysis of the rmsd between coordinates, of the Φ and Ψ dihedral angle distribution in a Ramachandran plot, and of the restraint violations. The protein structure is well-defined, with an average rmsd for the 31 final structures of 0.53 ± 0.07 Å for the backbone heavy atom coordinates in secondary structure elements and 1.47 ± 0.1 Å for all atoms (Table 1 and Figure 3). The good quality of the structures that were obtained results from a relatively high number of medium- and long-range NOE restraints involving side chain protons (about half of the total number), almost uniformly distributed over the sequence. The first and last α-helices (A and D) have relatively higher (by a factor of 2) rmsd values, probably due to the fraying effect of the fluctuating terminal segments. The second Ca^{2+} binding site is less defined mostly due to the lack of NOE restraints (251 for site I, relative to 171 for site II). This is in agreement with the above-mentioned observation of the persistence of a consensus hydrogen bond in site I.

The AQUA and PROCHECK-NMR programs (*16*) were used to assess the quality of the restraints and to determine the regularity of the geometry. More than 75% of the Φ and Ψ angle pairs of the 31 final structures lie in the most-favored region of the Ramachandran plot, and ~99% of them lie in the allowed regions. Asn26 is mostly found in the disallowed regions of the Ramachandran plot. This loop residue is not engaged in a detectable hydrogen bond and presumably undergoes some geometry constraint from the neighboring amino acids.

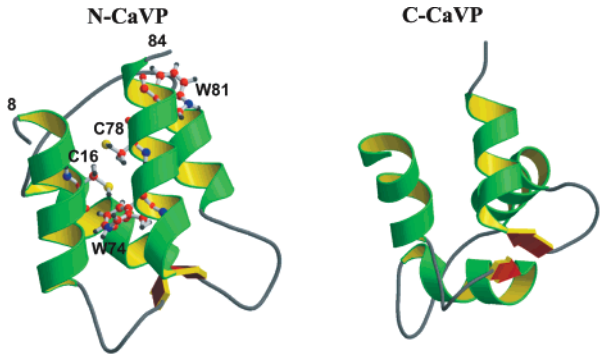

FIGURE 4: Global structure of N-CaVP and C-CaVP (Ca^{2+}-saturated) determined by NMR. The side chains of the Trp and Cys residues of N-CaVP are shown in a stick representation.

According to the rmsd values for the structure superposition, the optimized structures of N-CaVP are better defined than those previously determined for the Ca^{2+}-bound C-terminal domain (*8*). Other EF-hand domains, with a stable apo form, showed an improved structure in the absence of calcium (relative to the bound form), essentially due to a larger number of and a better quality of the NOE connectivities (*33*, *34*). Indeed, in the absence of bound calcium, the structure is more compact, allowing many contacts between hydrophobic side chains from the four α-helices and the *β*-sheet.

The tertiary structure consists of two EF-hand motifs, connected by a small antiparallel *β*-sheet (Figure 4). This intermotif *β*-sheet is conserved in all EF-hand domains independent of the presence or absence of bound ions, as was observed in CaM (*35*), sTnC (*36*), or calbindin D_{9k} (*29*).

Analysis of the interhelical angles in the EF-hand motifs provides a useful quantitative way of assessing the conformational changes or comparing structures of homologous proteins (*37*−*39*). The mean interhelical angles for site I (A and B) and II (C and D), determined for the 31 refined structures of N-CaVP, are 130 ± 4° and 168 ± 3°, respectively, considerably larger than those observed in the

Ca^{2+}-bound C-CaVP (Figure 4). The angles observed for site I fall in the range usually observed for apo-state domains, while site II exhibits one of the largest angles ever observed in the EF-hand family (*39*, *40*). The key structural feature of the regulatory domains in Ca^{2+} sensor proteins is the large conformational change from a compact closed state, in the absence of ions, to an active state with an open conformation, exposing hydrophobic patches, upon Ca^{2+} binding. In more quantitative terms, the interhelical angles in such EF-hand motifs decrease by ~45° (*41*). Due to its inability to bind metal ions, the N-CaVP domain exhibits a permanently closed conformation.

Accumulation of structural data on EF-hand proteins tends to demonstrate that the EF-hand domains are not simply divided into open or closed conformations, with two extreme values for the interhelical angles, but exhibit a multitude of unique conformational states, like a "continuum of conformations" (*39*) with subtle functional differences.

The hydrophobic core, including three aromatic amino acids (Phe20, Phe23, and Trp74) and several nonpolar aliphatic chains (Met17, Ile55, Met56, and Leu75), generates a dense network of long-range NOE connectivities, which proved to be very useful for the structure refinement. Furthermore, the strong NOE interactions between Ile55 (on helix C), Trp81 (helix D), and Tyr47 (linker) contribute to a better definition of the linker relative to the equivalent fragment in C-CaVP (*8*). The branched side chain of the completely buried Ile55 plays an important role in the stabilization of the tertiary structure displaying many contacts with hydrophobic residues of the core (especially aromatic), as reflected in the unusual high-field shift of some of its resonances (i.e., $H^{\gamma 11}$, −0.38 ppm; $H^{\gamma 12}$, −1.83 ppm; and $H^{\delta 1}$, −0.79 ppm).

The N-CaVP domain includes two cysteine residues, Cys16 and Cys78 on helices A and D, respectively. Expression of cysteine-bearing proteins in the *E. coli* cytoplasm, characterized by an efficient reductive environment, should maintain the sulfhydryl groups in a reduced state (*42*). During the purification procedure and recording of the spectra, we used a reducing agent (DTT) to prevent disulfide formation, especially those yielding to unsuitable intermolecular cross-linking. Actually, we found no tertiary distance restraint in the NOESY spectra which may indicate an eventual intramolecular disulfide formation. Analysis of the final structures showed that the average distance between the sulfur atoms from the two cysteines is ~3.65 Å (see Figure 4), which is longer than a disulfide bond, but short enough to be oxidized and form a disulfide bridge after minor side chain rearrangement. Incubation of the protein with different spin-labels (iodoacetamide or maleimide nitroxides) for various periods of time revealed that one Cys side chain per monomer could be slowly oxidized to give a mixed disulfide. Analysis of the EPR spectra of the spin-labeled protein showed that the correlation time of the nitroxide moieties varies from 0.1 to 1.2 ns, depending on the size of the reagent. These values are much smaller than the global rotational time of the protein (see below), indicating that the binding cavity is large enough to provide a high degree of flexibility to the bound reagent (*43*).

In contrast with the recombinant samples, the purified wild-type protein includes a well-protected disulfide bond (*44*). Therefore, the structural data presented here together with the recent functional studies on recombinant CaVP domains (*9*) demonstrate that the presence of the intramolecular disulfide bridge is not necessarily required for the proper folding or Ca^{2+} binding.

A similar pair of Cys residues, also situated on helices A and D, but not exactly in the same relative sequence positions, was observed in chicken cardiac TnC. Oxidation of the cysteines does not alter the domain structure (*45*, *46*) or the Ca^{2+} affinity of site II (site I is dead), but appears to change the Ca^{2+}-dependent function of the protein (*47*). In contrast, an extracellular Ca^{2+} binding motif (BM-40) has an intramotif disulfide bond that is critical for the global folding and affinity for the metal ion (*48*).

Fluorescence Studies. The two Trp residues of CaVP (Trp74 and Trp81) belong to the N-terminal domain, and both are placed on the D α-helix. As shown in Figure 4, the indole moieties have multiple contacts with other side chains, which may considerably restrict their movement. Therefore, the Trp fluorescence should shed light on the local mobility of aromatic moieties and also on the global protein dynamics.

Analysis of the time-resolved fluorescence data using the maximum entropy method provides information about the excited-state lifetime distribution and the characteristic times for anisotropy decay. Thus, the fluorescence decay of the two Trp residues at 340 nm (the maximum of fluorescence emission) and 25 °C exhibits three distinct components characterized by 0.21 ± 0.04, 0.93 ± 0.13, and 2.76 ± 0.10 ns with fractional populations of 12.6, 22.4, and 65.0%, respectively. Multicomponent behavior is often encountered, even in single Trp-bearing globular proteins studied so far (*49*), and is generally related to the existence of alternative conformations of the indole group (*50*−*52*) or to quenching of the excited state by a variety of movement-independent mechanisms (*53*). Since N-CaVP contains two Trp residues, the individual contribution of each indole moiety could eventually be evaluated by performing similar measurements at other emission wavelengths. Comparison of the fluorescence lifetime profiles at 315, 330, and 350 nm (Figure 5) showed a significant correlation between the lifetime distribution and emission wavelength; from 315 to 350 nm, the weight of the short lifetime component decreases and is slightly shifted toward longer lifetimes, while the contribution of the long lifetime component increases. This suggests that the contributions of the two Trp residues to the fluorescence emission may be distinguished. The short lifetime component should represent Trp74, which is completely embedded in the hydrophobic core (Figure 4) and exhibits a blue-shifted fluorescence. Inspection of the solution structure shows that the indole group of this residue is within 5.0 Å of a cysteine side chain (Cys78), a residue with an efficient quenching capacity (*54*). This may explain the short lifetime component. As the second tryptophan (Trp81) is more exposed to the solvent, its fluorescence emission should appear at longer wavelengths and should be associated with the longest lifetime component. The distinction between the two fluorescent residues is in agreement with the calculated accessible surface of the two side chains. Using the DSSP program (*55*) and the average NMR structure, one obtains areas of 1 $Å^2$ for Trp74 and 77 $Å^2$ for Trp81. This type of correlation between short-lived Trp excited-state populations and the blue emission, characteristic of buried indole moieties, is often encountered in two-Trp-containing proteins (*22*).

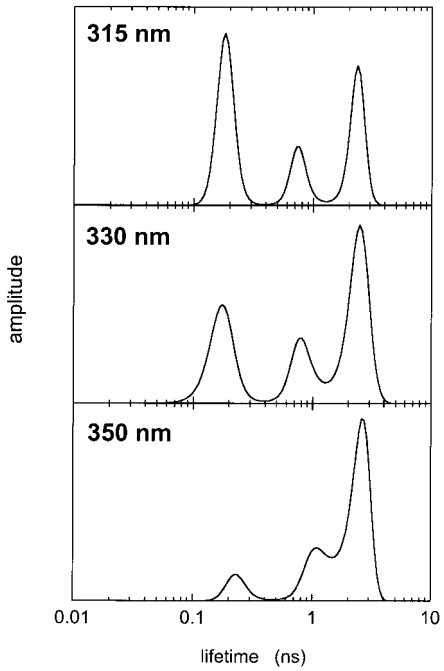

FIGURE 5: Maximum entropy method recovered lifetime distribution of Trp74 and Trp81 at three emission wavelengths. The centers (τ_i) and amplitudes (α_i) of peaks are as follows: $\tau_1 = 0.19$ ns ($\alpha_1 = 0.49$), $\tau_2 = 0.76$ ns ($\alpha_2 = 0.17$), and $\tau_3 = 2.32$ ns ($\alpha_3 = 0.35$) at 315 nm; $\tau_1 = 0.18$ ns ($\alpha_1 = 0.32$), $\tau_2 = 0.83$ ns ($\alpha_2 = 0.19$), and $\tau_3 = 2.41$ ns ($\alpha_3 = 0.49$) at 330 nm; and $\tau_1 = 0.24$ ns ($\alpha_1 = 0.10$), $\tau_2 = 1.08$ ns ($\alpha_2 = 0.23$), and $\tau_3 = 2.49$ ns ($\alpha_3 = 0.67$) at 350 nm. χ^2 values are 1.09 at 315 nm, 1.07 at 330 nm, and 0.97 at 350 nm.

The anisotropy decay curves, also analyzed by the maximum entropy method, enabled us to characterize the movement of the Trp residues. As long as the two side chains have a restricted movement, these data may provide information about the Brownian rotational diffusion of the protein as a whole. Analysis of the data at various emission wavelengths gives a major rotational correlation time population with center values comprised between 6 and 7 ns and an average of 6.8 ± 0.8 ns, which should characterize the rotational diffusion of the whole protein. Such a value for the rotational correlation time is larger than what may be expected for a reasonably hydrated (30−40%) isotropic monomer (4.1−4.4 ns).

A second rotational correlation time population is observed at the red edge of the emission spectrum, with a subnanosecond value. This dynamic parameter should describe the local motion of the more exposed tryptophan residue (Trp81). The associated order parameter (S^2) was estimated to be ~0.94, which, in a simple model of diffusion in a cone, would correspond to a wobbling angle of ~15°.

^{15}N Relaxation Parameters. Among the 81 non-proline residues of N-CaVP, the first three residues and residues Lys49, Arg50, and Lys67 were not unambiguously assigned. Due to superposition problems, the cross-peaks corresponding to residues Ile19, Phe23, and Gln45 were difficult to quantify. Therefore, we were able to collect relaxation data (R_1, R_2, and η) for 73 of the 86 residues (Figure 6).

The longitudinal relaxation rates (R_1) display a small variability along the sequence, with the majority of the values comprised between 1.92 and 2.34 s^{-1}, and an average over all residues of 2.1 ± 0.2 s^{-1}. The pattern of R2 is more

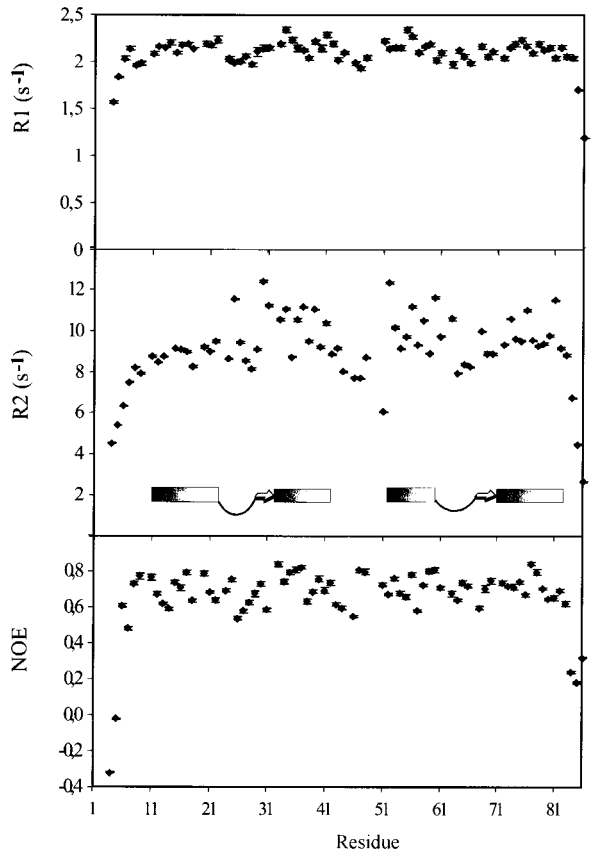

FIGURE 6: Experimental relaxation rates (R_1 and R_2) and the heteronuclear NOE (I_{sat}/I_{nonsat}) as functions of amino acid sequence of N-CaVP, measured at 11.74 T and 25 °C. The secondary structure elements determined from NMR analysis are shown in the middle of the figure.

variable along the protein sequence, with a mean value over all residues of 9.1 ± 1.7 s^{-1}. The heteronuclear steady-state NOEs (η = NOE − 1) display a small dispersion around the average value (−0.34). As for the pattern of the R_1 and R_2 relaxation rates, the N- and C-termini show significantly lower values, characteristic of flexible or poorly structured peptide fragments.

Correlation Time. Using the atomic coordinates of the average structure, we calculated first the components of the diagonalized tensor of the inertia momentum. Considering only the protein core, having a well-defined structure, we obtained a ratio of the relative moments of 1.00:0.82:0.70, indicating that the molecule has a slightly asymmetric shape. A test of the axially symmetric hypothesis, using the R_2/R_1 ratios in well-defined segments and the software developed by Dosset and coll. (*56*), showed no statistically significant improvement in the χ^2 value, relative to the isotropic case. Accordingly, N-CaVP is assumed to have only a small degree of diffusion anisotropy which may not affect considerably the microdynamic parameters, particularly the generalized order parameter (*57*). The isotropic global diffusion will therefore be considered a good model for N-CaVP under the present experimental conditions.

As the next step in the analysis of relaxation parameters, we calculated the isotropic correlation time of the Brownian diffusion, using a procedure designed to minimize the effect of eventual slow exchange processes (*20*). The estimated value is 7.1 ns which is within the limits normally found for proteins of this size (*58*), and is in good agreement with the

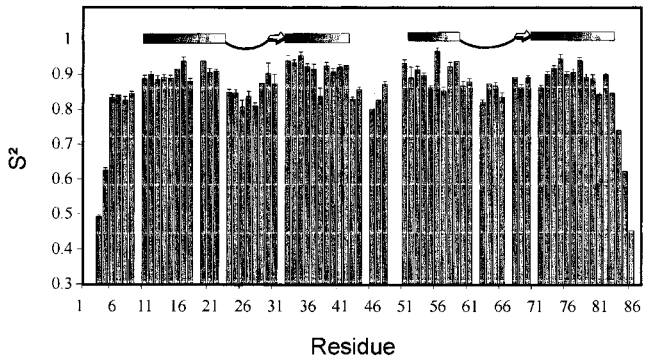

FIGURE 7: Backbone order parameters S^2 for N-CaVP. The secondary structure elements determined from NMR analysis are shown at the top of the figure.

value obtained by fluorescence analysis (mean value of 6.8 ns), despite the large difference in concentration (2 orders of magnitude). A similar agreement between NMR and fluorescence was recently reported for a mutant of carp parvalbumin (*59*), but alternative situations, in which the two techniques resulted in distinct correlation times, were also reported (*60*, *61*).

Dynamic Parameters. The motional parameters, which have a more phenomenological significance, were extracted from the relaxation data using the Lipari−Szabo "model-free" approach. Data were fitted by the simpler approach (S^2, τ_e, and R_{ex}) (*18*) for 66 residues and by the extended procedure (including slower internal movements) (*19*) for seven residues (Lys4, Ala5, Ala7, Thr46, Gln84, Asp85, and Asp86). Only small exchange contributions ($R_{ex} < 2$ Hz) were required for several amide groups.

The order parameter S^2 varies between 0 and 1, and characterizes the amplitude of the rapid internal motions on the picosecond to nanosecond time scale. $S^2 = 1$ indicates the absence of any internal motion (the molecule behaves like a rigid body), while $S^2 = 0$ represents a completely unrestricted rapid motion. The sequence distribution of the order parameters, calculated for an overall correlation time τ_c fixed at 7.1 ns, is shown in Figure 7. The average values for the α-helices [0.90 (A), 0.91 (B), 0.90 (C), and 0.89 (D)] are within the upper range of values generally obtained in other globular proteins (*58*). As usual, several residues at the N- and C-terminal ends exhibit large amplitude fluctuations on a time scale shorter than 1 ns, with order parameters down to 0.5. On the other hand, in the calcium binding loops and the intermotif linker, the H^N-N order parameters are moderately decreased relative to those of the helix fragments (but higher than 0.8), indicating that the fast movement of the backbone in these segments is less restricted.

A survey of previous dynamics studies on EF-hand proteins shows that the amplitude of rapid motions in the Ca^{2+}-bound loops is roughly the same as in the neighboring helices (*13*, *62*−*64*), which is in contrast with the apo form where the amplitude of fluctuations increases significantly (S^2 decreases down to 0.4) (*65*−*67*). However, the extent of the rapid flexibility changes on metal binding varies from one protein to another or between sites in the same domain, reflecting the entropic contribution to the Ca^{2+} binding free energy (*67*). The binding loops of the defunct EF-hand domain, studied here, exhibit the same dynamic trend (with reduced absolute changes) as the apo form of the functional domains studied so far. In contrast, the amplitude of the fast motion in the intermotif linker appears to be independent of the binding state but varies considerably among different domains (*63*, *64*, *68*). In N-CaVP, the S^2 variation in the linker is clearly smaller than in the holo C-CaVP domain, in agreement with more interresidue contacts and the better structural definition of this region in the first domain.

Analysis of the relaxation data of indole $N^{\epsilon 1}$ nitrogen nuclei, using an appropriate value for the chemical shift anisotropy $\Delta\sigma$ of −126 (*69*), enabled us to calculate the order parameters for the NH vectors in Trp74 and Trp81: 0.93 and 0.89, respectively. Despite their distinct solvent accessibility, the two aromatic side chains display a low-amplitude picosecond flexibility, comparable to that observed for the backbone amide groups. Trp74, deeply embedded in the hydrophobic core of the protein, is only slightly more constrained than the more exposed Trp81. Again, there is a very good agreement between the order parameters estimated from the relaxation data and the fluorescence anisotropy decay.

Interpretation of the internal correlation time (τ_e) is less straightforward than the order parameter, as it depends on both the rate and amplitude properties of the internal motion. The calculated τ_e values are distributed around 100 ps (the average is 105 ps), as in many other EF-hand proteins (*66*, *67*).

Study of the amide hydrogen−deuterium exchange is an alternative, powerful method for the investigation of local or global dynamic processes in biopolymers. In contrast with the C-terminal domain, where the slow proton exchange rates were used to identify the hydrogen bonds in stable secondary structure elements (*8*), the N-CaVP shows only fast amide exchange which could not be monitored by recording real-time spectra. Three main structural mechanisms are currently invoked to explain the hydrogen exchange in proteins: local fluctuations, subglobal or regional unfolding, and transient whole-molecule unfolding (*70*). Given the low unfolding transition temperature of N-CaVP (44 °C) (*9*), one may consider that the dynamic equilibrium between folded and unfolded structures at 25 °C may account for a large part of the fast hydrogen exchange. These large-scale conformational fluctuations, usually on a time scale of microseconds or longer, represent an additional flexibility mode which completes the dynamic description of the N-terminal domain.

Functional Implications. Analysis of structure−function relationships in the calcium sensor proteins suggested that the domains may be classified as structural or regulatory units, according to the conformational sensitivity to metal binding and the capacity of target activation (*71*, *72*). The regulatory domains (N- and C-terminal domains of CaM, and N-terminal domains of TnC and recoverin) bind Ca^{2+} after a stimulation signal, undergo a conformational change, and activate a target molecule. In contrast, the structural domains are always Ca^{2+}-bound (C-termini of TnC and recoverin) and show an only minor contribution to the interaction with other proteins. Recent structural information about new calcium proteins extends this simplified picture, adding more complexity to the structure−function relationships of EF-hand proteins. Thus, S100A10, a homodimer of EF-hand pairs that lost the calcium binding capacity, is still able to bind a target molecule (annexin II N-terminal peptide) without major conformational changes (*73*). Other sensor

proteins from the very diverse S100 subfamily display closed-type interhelical angles and undergo only minor changes upon Ca^{2+} binding (*74*).

In the case of CaVP, the C-terminal half could be considered a regulatory domain (*8*) while N-CaVP may represent a new type of structural domain with nonbinding EF-hand motifs, a closed structure, and a minor contribution to the target binding. Indeed, recent biochemical experiments (*9*) showed that the C-terminal domain of CaVP recognizes and interacts strongly with the CaVPT, but with an affinity lower than that of the intact protein. This indicates that N-CaVP also contribute, albeit to a lesser extent, to the complex formation. In the Ca^{2+}-saturated state, the C-terminal lobe is in an open state, contributing with a large hydrophobic patch to the intermolecular interaction surface. In contrast, due to its closed conformation, the N-terminal lobe is not able to grip to the target but may add only a few contacts to stabilize the complex. In fact, analysis of the accessible surface of N-CaVP showed that its hydrophobic component is as high as in the bound C-CaVP, the difference being that it is not localized in a small area but is distributed quite uniformly on the whole surface. Thus, the defunct domain may provide some apolar interacting sites with the CaVPT which can explain the difference between C-CaVP and CaVP in their affinity for the target molecule.

This picture has some similarities with the interaction mode between the heavy chain and the N-terminal domain of the essential light chain in the scallop myosin (*75*) or between the N-terminal lobe of sTnC (skeletal muscle) and a fragment of TnI (*76*). These EF-hand domains are also closed (despite a bound Ca^{2+} ion in the case of scallop myosin), and make several specific contacts with a helical region of the target sequence. The number of intermolecular interactions is significantly lower relative to those involving the C-terminal domains, suggesting that their role is to anchor, rather than to recognize, the target protein.

A more feasible comparison between CaVP function and that of its related proteins of the EF-hand family requires more precise data on the structural and energetic aspects of its intermolecular interactions. NMR and calorimetric experiments designed to explore the complex formation with artificial or natural targets are in progress in our laboratory.

ACKNOWLEDGMENT

We thank Yann Henry for help with the electron paramagnetic resonance experiments.

SUPPORTING INFORMATION AVAILABLE

Table S1 listing ^{15}N relaxation parameters (R_1, R_2, and η) of N-CaVP at 500 MHz and 25 °C. This material is available free of charge via the Internet at http://pubs.acs.org.

REFERENCES

1. Cox, J. A. (1986) *J. Biol. Chem. 261*, 13173−13178.
2. Zimmer, C. (2000) *Science 287*, 1576−1579.
3. Takagi, T., and Cox, J. A. (1990) *J. Biol. Chem. 265*, 19721−19727.
4. Petrova, T. V., Comte, M., Takagi, T., and Cox, J. A. (1995) *Biochemistry 34*, 312−318.
5. Kawasaki, H., Nakayama, S., and Kretsinger, R. H. (1998) *BioMetals 11*, 277−295.
6. Yuasa, H. J., Cox, J. A., and Takagi, T. (1999) *J. Biochem. 126*, 572−577.
7. Cox, J. A., Alard, P., and Schaad, O. (1990) *Protein Eng. 4*, 23−32.
8. Théret, I., Baladi, S., Cox, J. A., Sakamoto, H., and Craescu, C. T. (2000) *Biochemistry 39*, 7920−7926.
9. Baladi, S., Tsvetkov, P. O., Petrova, T. V., Takagi, T., Sakamoto, H., Lobachov, V. M., Makarov, A. A., and Cox, J. A. (2001) *Protein Sci. 10*, 771−778.
10. Falke, J. J., Drake, S. K., Hazard, A. L., and Peersen, O. B. (1994) *Q. Rev. Biophys. 27*, 219−290.
11. Kragelund, B. B., Jönsson, M., Bifulco, G., Chazin, W. J., Nilsson, H., Finn, B. E., and Linse, S. (1998) *Biochemistry 37*, 8926−8937.
12. Browne, J. P., Strom, M., Martin, S. R., and Bayley, P. M. (1997) *Biochemistry 36*, 9550−9561.
13. Théret, I., Cox, J. A., Mispelter, J., and Craescu, C. T. (2001) *Protein Sci. 10*, 1393−1402.
14. Cavanagh, J., Fairbrother, W. J., Palmer, A. G., III, and Skelton, N. J. (1996) *Protein NMR Spectroscopy. Principles and Practice*, Academic Press, San Diego.
15. Chylla, R. A., and Markley, J. L. (1993) *J. Magn. Reson., Ser. B 102*, 148−154.
16. Laskowski, R. A., Rullmann, J., Antoon, C., MacArthur, M. W., Kaptein, R., and Thornton, J. M. (1996) *J. Biomol. NMR 8*, 477−486.
17. Farrow, N. A., Muhandiram, R., Singer, A. U., Pascal, S. M., Kay, C. M., Gish, G., Shoelson, S. E., Pawson, T., Forman-Kay, J. D., and Kay, L. E. (1994) *Biochemistry 33*, 5984−6003.
18. Lipari, G., and Szabo, A. (1982) *J. Am. Chem. Soc. 104*, 4546−4559.
19. Clore, G. M., Szabo, A., Bax, A., Kay, L. E., Driscoll, P. C., and Gronenborn, A. M. (1990) *J. Am. Chem. Soc. 112*, 4989−4991.
20. Mispelter, J., Izadi-Pruneyre, N., Quiniou, E., and Adjadj, E. (2000) *J. Magn. Reson. 143*, 229−232.
21. Vincent, M., Gallay, J., and Demchenko, A. P. (1995) *J. Phys. Chem. 99*, 14934−14941.
22. Rouvière, N., Vincent, M., Craescu, C. T., and Gallay, J. (1997) *Biochemistry 36*, 7339−7352.
23. Tsuda, S., Miura, A., Gagné, S. M., Spyracopoulos, L., and Sykes, B. D. (1999) *Biochemistry 38*, 5693−5700.
24. Boyd, J., Dobson, C. M., and Redfield, C. (1985) *FEBS Lett. 186*, 35−40.
25. Strynadka, N. C., and James, M. N. G. (1989) *Annu. Rev. Biochem. 58*, 951−991.
26. Tsuda, S., Hasegawa, Y., Yoshida, M., Yagi, K., and Hikichi, K. (1988) *Biochemistry 27*, 4120−4126.
27. Krudy, G. A., Brito, R. M. M., Putkey, J. A., and Rosevear, P. R. (1992) *Biochemistry 31*, 1595−1602.
28. Ikura, M., Minowa, O., Yazawa, M., Yagi, K., and Hikichi, K. (1987) *FEBS Lett. 219*, 17−21.
29. Skelton, N. J., Kördel, J., and Chazin, W. J. (1995) *J. Mol. Biol. 249*, 441−462.
30. Malmendal, A., Evenäs, J., Forsén, S., and Akke, M. (1999) *J. Mol. Biol. 293*, 883−899.
31. Biekovsky, R. R., Martin, S. R., Browne, J. P., Bayley, P. M., and Feeney, J. (1998) *Biochemistry 37*, 7617−7629.
32. Wishart, D. S., Sykes, B. D., and Richards, F. M. (1992) *Biochemistry 31*, 1647−1651.
33. Finn, B. E., Evenäs, J., Drakenberg, T., Waltho, J. P., Thulin, E., and Forsén, S. (1995) *Nat. Struct. Biol. 2*, 777−783.
34. Gagné, S. M., Tsuda, S., Li, M. X., Smillie, L. B., and Sykes, B. D. (1995) *Nat. Struct. Biol. 2*, 784−789.
35. Zhang, M., Tanaka, T., and Ikura, M. (1995) *Nat. Struct. Biol. 2*, 758−767.
36. Herzberg, O., and James, M. N. G. (1988) *J. Mol. Biol. 203*, 761−779.
37. Nelson, M. R., and Chazin, W. J. (1998) *Protein Sci. 7*, 270−282.
38. Gagné, S. M., Li, M. X., McKay, R. T., and Sykes, B. D. (1998) *Biochem. Cell. Biol. 76*, 302−312.

39. Yap, K. L., Ames, J. B., Swindells, M. B., and Ikura, M. (1999) *Proteins: Struct., Funct., Genet. 37*, 499−507.
40. Kilby, P. M., Van Eldik, L. J., and Roberts, G. C. K. (1996) *Structure 4*, 1041−1052.
41. Gagné, S. M., Li, M. X., and Sykes, B. D. (1997) *Biochemistry 36*, 4386−4392.
42. Prinz, W. A., Åslund, F., Holmgren, A., and Beckwith, J. (1997) *J. Biol. Chem. 272*, 15661−15667.
43. Morrisett, J. D. (1976) *The use of spin labels for studying the structure and function of enzymes*, Vol. I, Academic Press, New York.
44. Kobayashi, T., Takagi, T., Konishi, K., and Cox, J. A. (1987) *J. Mol. Biol. 262*, 2613−2623.
45. Sia, S. K., Li, M. X., Spyracopoulos, L., Gagné, S. M., Liu, W., Putkey, J. A., and Sykes, B. D. (1997) *J. Biol. Chem. 272*, 18216−18221.
46. Pääkkönen, K., Annila, A., Sorsa, T., Pollesello, P., Tilgmann, C., Kilpeläinen, I., Karisola, P., Ulmanen, I., and Drakenberg, T. (1998) *J. Biol. Chem. 273*, 15633−15638.
47. Putkey, J. A., Dotson, D. G., and Mouawad, P. (1993) *J. Mol. Biol. 268*, 6827−6830.
48. Hohenester, E., Maurer, P., Hohenadl, C., Timpl, R., Jansonius, J. N., and Engel, J. (1996) *Nat. Struct. Biol. 3*, 67−73.
49. Lakovitz, J. R. (1999) *Principles of Fluorescence Spectroscopy*, 2nd ed., Kluwer Academic/Plenum, New York.
50. Willis, K. J., Neugebauer, W., Sikorska, M., and Szabo, A. G. (1994) *Biophys. J. 66*, 1623−1630.
51. Silva, N. D., and Prendergast, F. G. (1996) *Biophys. J. 70*, 1122−1137.
52. Ross, J. B. A., Wyssbrod, H. R., Porter, R. A., Schwartz, G. P., Michaels, C. A., and Laws, W. R. (1992) *Biochemistry 31*, 1585−1594.
53. Bajzer, Z., and Prendergast, F. G. (1993) *Biophys. J. 65*, 2313−2323.
54. Chen, Y., and Barkley, M. D. (1998) *Biochemistry 37*, 9976−9982.
55. Kabsch, W., and Sander, C. (1983) *Biopolymers 22*, 2577−2637.
56. Dosset, P., Hus, J.-C., Blackledge, M., and Marion, D. (2000) *J. Biomol. NMR 16*, 23−28.
57. Tjandra, N., Feller, S. E., Pastor, R. W., and Bax, A. (1995) *J. Am. Chem. Soc. 117*, 12562−12566.
58. Goodman, J. L., Pagel, M. D., and Stone, M. J. (2000) *J. Mol. Biol. 295*, 963−978.
59. Moncrieffe, M. C., Juranic, N., Kemple, M. D., Potter, J. D., Macura, S., and Prendergast, F. G. (2000) *J. Mol. Biol. 297*, 147−163.
60. Palmer, A. G., III, Hochstrasser, R. A., Millar, D. P., Rance, M., and Wright, P. E. (1993) *J. Am. Chem. Soc. 115*, 6333−6345.
61. Kemple, M. D., Buckley, P., Yuan, P., and Prendergast, F. G. (1997) *Biochemistry 36*, 1678−1688.
62. Kördel, J., Skelton, N. J., Akke, M., Palmer, A. G., III, and Chazin, W. J. (1992) *Biochemistry 31*, 4856−4866.
63. Barbato, G., Ikura, M., Kay, L. E., Pastor, R. W., and Bax, A. (1992) *Biochemistry 31*, 5269−5278.
64. Baldellon, C., Alattia, J.-R., Strub, M.-P., Pauls, T., Berchtold, M. W., Cavé, A., and Padilla, A. (1998) *Biochemistry 37*, 9964−9975.
65. Akke, M., Skelton, N. J., Kördel, J., Palmer, A. G., III, and Chazin, W. J. (1993) *Biochemistry 32*, 9832−9844.
66. Spyracopoulos, L., Gagné, S. L., Li, M. X., and Sykes, B. D. (1998) *Biochemistry 37*, 18032−18044.
67. Gagné, S. M., Tsuda, S., Spyracopoulos, L., Kay, L. E., and Sykes, B. D. (1998) *J. Mol. Biol. 278*, 667−686.
68. Mäler, L., Blankenship, J., Rance, M., and Chazin, W. J. (2000) *Nat. Struct. Biol. 7*, 245−250.
69. Hu, W., Lazo, N. D., and Cross, T. A. (1995) *Biochemistry 34*, 14138−14146.
70. Englander, S. W., Sosnick, T. R., Englander, J. J., and Mayne, L. (1996) *Curr. Opin. Struct. Biol. 6*, 18−23.
71. da Silva, A. C., and Reinach, F. C. (1991) *Trends Biochem. Sci. 16*, 53−57.
72. Ikura, M. (1996) *Trends Biochem. Sci. 21*, 14−17.
73. Réty, S., Sopkova, J., Renouard, M., Osterloh, D., Gerke, V., Tabaries, S., Russo-Marie, F., and Lewit-Bentley, A. (1999) *Nat. Struct. Biol. 6*, 89−95.
74. Mäler, L., Potts, B. C. M., and Chazin, W. J. (1999) *J. Biomol. NMR 13*, 233−247.
75. Houdusse, A., and Cohen, C. (1996) *Structure 4*, 21−32.
76. Vassylyev, D. G., Takeda, S., Wakatsuki, S., Maeda, K., and Maeda, Y. (1998) *Proc. Natl. Acad. Sci. U.S.A. 95*, 4847−4852.

BI011444Q